J. Fluid Mech. (2001), *vol.* 436, *pp.* 231–248. Printed in the United Kingdom

Longitudinal and transverse structure functions in a turbulent round jet: effect of initial conditions and Reynolds number

By G. P. ROMANO[1] AND R. A. ANTONIA[2]

[1]Department of Mechanics and Aeronautics, 'La Sapienza' University, 00184 Rome, Italy
[2]Department of Mechanical Engineering, University of Newcastle, NSW, 2308, Australia

(Received 28 February 2000 and in revised form 25 September 2000)

The difference between scaling exponents of longitudinal and transverse velocity structure functions in the far-field of a round jet is found to depend on the anisotropy of the flow. The effect of the large-scale anisotropy is assessed by considering different initial conditions at the jet nozzle, and hence different ratios of the longitudinal to transverse rms velocities. The effect of the Taylor microscale Reynolds number on the small scale anisotropy is also considered. Both effects account, to a large extent, for the observed difference between longitudinal and transverse exponents and the disagreement between previously published results of different authors. This disagreement also depends on the method used to determine the inertial range. An empirical description of the overall behaviour of the structure functions provides reasonable estimates for the longitudinal and transverse exponents, accounting reasonably well for the anisotropy of both large- and small-scale motions.

1. Introduction

It is well established that moments of the increment between velocity fluctuations at two points (or velocity structure functions (SF)) in a high-Reynolds-number turbulent flow scale as a power of the separation between the points, e.g. Frisch (1995). According to the local similarity hypothesis of Kolmogorov (1941, hereinafter K41), the scaling exponent increases linearly with the moment of the SF. In reality, the increase is nonlinear owing to fluctuations of the energy dissipation rate, a phenomenon usually referred to as small-scale intermittency. Departures from K41 have been extensively reported especially for longitudinal structure functions (LSF), that is for the statistics of the differences of velocity fluctuation components along the direction of separation (e.g. Sreenivasan & Antonia 1997). The departure is reasonably well described by a nonlinear behaviour, the details of which depend on the intermittency model that is used, e.g. Frisch (1995). Less attention has been given to transverse structure functions (TSF) or differences of velocity components along directions orthogonal to the separation. Especially for anisotropic flows, a complete investigation of intermittency effects must include information with respect to both longitudinal and transverse directions. For locally isotropic incompressible turbulence, the second-order LSF and TSF are related by (e.g. Monin & Yaglom 1975)

$$\langle (\delta u_T^*)^2 \rangle = \left(1 + \tfrac{1}{2} r^* \frac{\partial}{\partial r^*}\right) \langle (\delta u_L^*)^2 \rangle, \tag{1}$$

where $\delta\alpha \equiv \alpha(x+r) - \alpha(x)$ and α stands for either u_L, the velocity fluctuation in the same direction as r, or u_T, the velocity fluctuation normal to that of r. The asterisks in (1) denote normalization by the Kolmogorov lengthscale η ($\equiv (\nu^3/\langle\epsilon\rangle)^{1/4}$ where $\langle\epsilon\rangle$ is the mean turbulent energy dissipation rate) and/or the Kolmogorov velocity scale u_K [$\equiv (\nu\langle\epsilon\rangle)^{1/4}$]. In the inertial range (IR) ($\eta \ll r \ll L$, where L is the integral length scale),

$$\langle(\delta\alpha^*)^p\rangle \sim C_\alpha(p)\, r^{*\zeta_p^\alpha},$$

where $C_\alpha(p)$ may, in general, depend on the flow macrostructure (K41). The use of (1) implies that the scaling exponents are related by

$$\zeta_2^T = \zeta_2^L + \log_{r^*}\left[\frac{C_L(2)}{C_T(2)}(1 + \tfrac{1}{2}\zeta_2^L)\right]. \tag{2}$$

(the argument of the logarithm to base r^* is usually assumed to be equal to 1 and the equality between ζ_2^T and ζ_2^L follows). When the same velocity fluctuation, for example u, is used to form both LSF and TSF, we may expect the difference between ζ^L and ζ^T to be small, especially when the separation is along a homogeneous flow direction (Noullez *et al.* 1997; van de Water & Herweijer 1999; Zhou, Pearson & Antonia 2000). In the latter case, $\langle(\delta u_L)^2\rangle = \langle(\delta u_T)^2\rangle$ when r is sufficiently large for the velocity fluctuation at the two points to become decorrelated. Results comparable to (1) and (2) have yet to be rigorously established for $p = 4$.

Equations (1) and (2) can be used to assess which scales conform with isotropy and allow isotropic values of the transverse exponents to be estimated from measured longitudinal exponents. These isotropic values can be compared with the measured transverse exponents. If we assume that $\zeta_p^L = \frac{1}{3}p$, as in K41, but allow for the possibility, contrary to K41, that ζ_p^L may differ from ζ_p^T, the equality

$$\zeta_2^L = \zeta_2^T \tag{3}$$

follows from (2). Deviations from (3) owing to intermittency corrections are small (less than 1%) and the argument of the logarithm remains close to 1. Indeed, a larger difference should exist between ζ_2^T and ζ_2^L if the argument differs significantly from 1, i.e. if the ratio $C_T(2)/C_L(2)$ differs from 4/3. Atmospheric surface layer data (Antonia & Pearson 1999) suggest that the value of 4/3 may indeed be approached when $R_\lambda \simeq 10^4$. An extrapolation of (3) to $p \neq 4$ may lead to the conclusion that the absolute magnitudes of the LSF and TSF scaling exponents are equal. This result is not supported by the majority of the available experimental and numerical data. In particular, there is only moderate support for (3) (Noullez *et al.* 1997), whereas there is significant evidence to suggest that ζ_p^T is smaller than ζ_p^L (Boratav & Pelz 1997; Camussi, Barbagallo & Guj 1997; van de Water & Herweijer 1999; Zhou & Antonia 2000). The difference is typically about 20% for $p = 4$ and 40% for $p = 8$. The reasons for this inequality clearly require further investigation, especially in the context of improving small-scale turbulence modelling. Possible explanations, not necessarily unrelated, for this inequality are listed below:

(i) the anisotropy of the flow;
(ii) the effect of Reynolds number;
(iii) the effect of initial and boundary conditions;
(iv) the intermittencies affecting LSF and TSF (which may be inherently different).

Possibility (i) seems to be a natural source for the observed differences. Equation (1) can help to quantify this effect. While this is the approach adopted here, other interesting approaches have been considered in the literature. For example, con-

ditioning on the large-scale velocity fluctuation was used by Sreenivasan & Dhruva (1998) to account for the effect of the mean shear on the anisotropy of the IR. More recently, the isotropic part of the measured structure functions was extracted (Kurien & Sreenivasan 2000) by projecting these functions onto the isotropic sector of the so-called SO(3) decomposition (e.g. L'vov & Procaccia 1996). Regarding (ii), there is a tendency for the IR to contract and eventually disappear as the Reynolds number is reduced. This may affect TSF more than LSF, leading to a biased evaluation of the scaling exponents. Pearson & Antonia (1999, 2001) found that the magnitude of the difference $\zeta_p^L - \zeta_p^T$ decreases as R_λ (the Taylor microscale Reynolds number $= u'\lambda/\nu$; u is the longitudinal velocity fluctuation, λ is the longitudinal Taylor microscale and a prime denotes the r.m.s. value) increases, although it does not completely vanish even at $R_\lambda \simeq 10\,000$, see also Dhruva, Tsuji & Sreenivasan (1997). Although George (1989) has questioned the universality of similarity solutions in jet flows when different initial conditions are involved, (iii) has yet to be investigated systematically; this effect may result in different injections of energy at the large scales which could, in turn, affect the IR. Such a scenario could explain why there is generally qualitative agreement with the inequality $\zeta_p^T < \zeta_p^L$ as well as significant disagreement with regard to its magnitude. Possibility (iv) has been considered by some authors, in particular through possible differences in the scaling of the locally averaged energy dissipation rate and of the enstrophy. It has been suggested, on the basis of DNS data (e.g. Chen *et al.* 1997; Boratav & Pelz 1997) that δu_L is principally influenced by the former, whereas δu_T depends mainly on the latter. Using grid turbulence measurements ($R_\lambda < 100$), Antonia, Zhou & Zhu (1998; also Zhou & Antonia 2000) inferred the LSF and TSF exponents from those of the energy dissipation rate and enstrophy, respectively. The resulting differences, 2% for $p = 4$ and 6% for $p = 8$, were much smaller than the measured differences. Paret & Tabeling (1998) have noted that incompressibility could also cause LSF and TSF exponents to be different, owing to different forms of the longitudinal and transverse correlations.

The main aim of the paper is to investigate the difference between scaling exponents of LSF and TSF in the context of a round jet, for which the anisotropy associated with the large-scale motion is likely to be more important than in grid turbulence. The attention is focused on the effect of both large- and small-scale anisotropies, the former through the velocity fluctuations and the latter through the Reynolds number. Different velocity fluctuations are considered by comparing results in two jets with different initial conditions, one using water and the other air, at the same x/d location and nominally the same R_λ ($\simeq 500$). At this location, the large-scale anisotropy is different in each flow, reflecting differences in the way the two facilities are designed and constructed. Measurements are also made at the same x/d, but over a significant R_λ range in each of the two jets.

2. Experimental facilities

2.1. *Air jet*

The air jet facility consists of an open circuit wind tunnel. Air is supplied by a variable speed centrifugal blower through a diffuser, a settling chamber and a (1 : 85 in area) contraction with an exit diameter d equal to 55 mm. An air filter at the inlet to the blower minimizes the contamination of the flow by dust particles. The blower is coupled to a three-phase 415 V, 50 Hz a.c. motor controlled by a variable-frequency electric converter driver. A flexible rubber section was installed between the blower–

motor assembly and the settling chamber in order to reduce any transmission of vibration generated by the assembly. A series of screens and a honeycomb section, constructed from drinking straws, were inserted in the settling chamber to reduce the turbulence level and straighten the flow. The jet exhausts into the ambient air of a relatively large laboratory. A cross-wire probe was mounted on a two-dimensional traversing mechanism. The hot wires were etched from Pt–10% Rh to a diameter of 2.5 μm and an active length of about 0.5 mm (about 3.3 Kolmogorov microscales at the measurement station). In-house constant temperature anemometers were used to operate the wires at an overheat ratio of 1.5. The wires were calibrated for velocity and yaw at the nozzle end plane using a Pitot tube connected to a Furness micromanometer. The anemometer signals were digitized at a sampling frequency f_s using a 12-bit analogue–digital board into a PC.

2.2. *Water jet*

In the closed circuit facility, a centrifugal pump moves water from a primary tank into a settling chamber which is equipped with a valve to dampen oscillations due to the pump. Screens and honeycombs are placed at the end of the chamber before the first contraction (1 : 15 in area) which leads to a rectangular section. A second contraction (1 : 3 in area) provides the transition to a 1.5 m long pipe, with an inner diameter of 14 cm. It is followed by a third contraction. (1 : 50 in area). This severe contraction was designed to suppress the growth of Görtler vortices; it consists of adjacent truncated conical sections joined by smoothed corners. The jet (diameter $d = 20$ mm) exits into a large water-filled tank (height 30d, width 30d, length 60d) from which the water returns to the primary tank. The pipe, contraction and large tank are made of Perspex to allow unimpeded optical access to the flow. At the jet exit, the flow is axisymmetric and has no swirl; preliminary measurements also confirmed that it is unaffected by any external forcing due to the pump. Two-component forward-scatter mode Laser-Doppler anemometer (LDA) measurements were made using a He–Ne laser system equipped with two Bragg cells. The fringe spacing was 3.416 μm and the measurement volume size is about 0.1 mm, 0.1 mm and 0.8 mm along the x-, y- and z-axes, respectively. The LDA data are resampled using a linear interpolation to obtain equispaced samples which also provide unbiased statistics. The value of R_λ is sufficiently large to expect the LDA noise not to affect the behaviour of structure functions in the IR (Antonia *et al.* 1997*b*). The noise contribution to LDA measurements is evaluated using the well-known theoretical results in the dissipative range (DR) (Romano, Antonia & Zhou 1999). The influence of this noise is estimated to be restricted to the region $r^* < 50$ (it is investigated in more detail in § 4).

3. Experimental conditions

In each jet, measurements were made at $x/d \simeq 40$ (x is measured from the nozzle exit plane), where the flow field may be considered to be approximately self-preserving. The jet exit velocity U_j was selected so that R_λ was nominally the same ($\simeq 495$ and 500 in the air and water jets, respectively) at the measurement location. To achieve this, the exit Reynolds number $R_j \equiv U_j d/\nu$ was 1.7×10^5 for the air jet and 4.9×10^4 in the water jet. The different values of R_j reflect a difference in the initial conditions and characteristic development of the two flows. Antonia, Satyapra Kash & Hussain (1980) proposed empirical expressions relating R_λ in the self-preserving region of plane and circular jets to R_j. Typically, the relations are of the form $R_\lambda = kR_j^{1/2}$, where the constant k embodies several effects of the local turbulence intensity u'/U_0 (U_0 is the

	Air	Water
R_λ	495	500
u'/U_0	0.26	0.29
v'/U_0	0.22	0.22
u'/v'	1.18	1.32
$\langle\epsilon\rangle L_u/u'^3$	0.76	0.35
$k \equiv R_\lambda/R_j^{1/2}$	1.2	2.3
$k_1 \equiv (U_0/U_j)(x/d)$	6.64	6.70
$k_2 \equiv L_0/x$	0.104	0.086
η (mm)	0.105	0.10
u_K (m s^{-1})	0.099	0.011
L_u (m)	0.166	0.055
L_v (m)	0.071	0.025
Independent samples	15 000	8000

TABLE 1. Characteristic parameters for the two jets at $x/d = 40$.

local mean velocity, also on the axis; the external 'free stream' velocity is negligibly small in each jet), the dimensionless mean energy dissipation rate $\langle\epsilon\rangle L_0/U_0^3$ (L_0 is the half-radius) as well as of factors such as $\mathrm{d}L_0/\mathrm{d}x$ and $\mathrm{d}U_0/\mathrm{d}x$, which characterize the streamwise development of the jet. These parameters, together with the ratio v'/U_0 (v' is the radial r.m.s. velocity on the axis) and the integral lengthscales L_u and L_v, associated with components (u and v) are shown in table 1. L_u and L_v are inferred, using the Taylor hypothesis from integrations up to the first zero-crossing point of the u and v autocorrelations. For example, $L_u = \langle U\rangle \int_0^{\tau_0} \rho_{uu}(\tau)\,\mathrm{d}\tau$ where $\rho_{uu}(\tau)$ is the temporal longitudinal autocorrelation function and τ_0 is the time corresponding to the first zero crossing of $\rho_{uu}(\tau)$.

The table indicates important differences between the two jets. These differences are reflected in the significantly different values of k and $\langle\epsilon\rangle L/u'^3$. $\langle\epsilon\rangle$ was estimated with the use of the isotropic relation $\langle\epsilon\rangle = 15\nu\langle(\partial u/\partial x)^2\rangle$ whereas $\langle(\partial u/\partial x)^2\rangle$ was inferred from the integral $\int_0^\infty k_1^2\phi_u(k_1)\,\mathrm{d}k_1$, where k_1 is the one-dimensional wavenumber and $\phi_u(k_1)$ is the spectral density of u ($\int_0^\infty \phi_u(k_1)\,\mathrm{d}k_1 = \langle u^2\rangle$) after the high-wavenumber noise contamination was removed (Pearson 1999). The difference in u'/v' (1.18 for the air jet and 1.32 for the water jet) is a measure of the different contributions from the large scales between the two jets. At the air jet nozzle exit, the velocity has a top-hat distribution. The boundary layer is laminar with a velocity profile in close, but not perfect, agreement with the Blasius solution; the boundary-layer shape parameter H is 2.63, compared to 2.59 for Blasius. The ratio u'/U_j is about 0.015 on the jet axis. The water jet also has a top-hat velocity profile at the nozzle exit. The boundary-layer shape parameter is equal to 3.29 and u'/U_j is about 0.021 on the jet axis.

The number of collected samples is about 10^6 in each jet. However, the number of independent samples, given by $\langle U\rangle T_S/2L_u$ (where T_S is the total record duration), is about 10^4 (the precise values are given in table 1).

4. Structure functions

The Taylor hypothesis has been used to convert the temporal SF to a spatial SF. The LSF is obtained from temporal differences of u, whereas the TSF is inferred from temporal differences of v. Second-order LSF and TSF are shown in figure 1 for the air jet. Also included in the figure is the second-order TSF calculated using equation

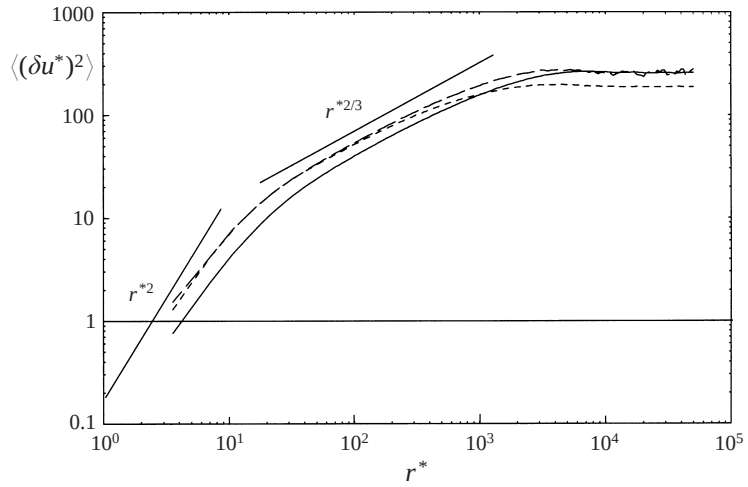

FIGURE 1. Measured second-order LSF and TSF for the air jet. The second-order TSF is also obtained from equation (1). Theoretical slopes in dissipative and inertial ranges are shown. ——, measured LSF; - - -, measured TSF; – –, TSF obtained with (1).

(1). The LSF distribution approaches the isotropic limit $r^{*2}/15$ at small r^*. This is expected since $\langle\epsilon\rangle = 15\nu\langle(\partial u/\partial x)^2\rangle$ was used to determine $\langle\epsilon\rangle$. The slope of the LSF is close to K41 ($p = 2/3$) over the IR, which extends from $r^* \simeq 50$ to $r^* \simeq 200$ (the identification of the IR is discussed in § 5). The TSF distribution approaches a limit which is somewhat smaller than $2r^{*2}/15$ at small r^*, reflecting a small departure from local isotropy. The ratio $\langle(\partial v/\partial x)^2\rangle/\langle(\partial u/\partial x)^2\rangle$ is 1.9 instead of 2 (isotropy). Over the IR, the slope indicated by the TSF distribution is noticeably smaller than that predicted by K41. The TSF distribution calculated using (1) follows the measured distribution reasonably well over the DR and the first part of the IR; the divergence between calculated and measured distributions is not surprising since, in the limit $r^* \to \infty$, equation (1) requires that $\langle(\delta v)^2\rangle = \langle(\delta u)^2\rangle$, i.e. $\langle v^2\rangle = \langle u^2\rangle$, whereas, in reality, the large-scale anisotropy enforces the inequality $\langle v^2\rangle < \langle u^2\rangle$. The u' and v' values in table 1 indicate that $\langle v^2\rangle/\langle u^2\rangle \simeq 0.72$ for the air jet. This large-scale anisotropy is, not surprisingly, larger than that indicated by the ratio $\langle(\partial v/\partial x)^2\rangle/\langle(\partial u/\partial x)^2\rangle$.

LSF and TSF distributions in the water jet are shown in figure 2. Overall, there is similarity between these distributions and those for the air jet, but the small-scale behaviour ($r^* < 10$) is now masked by a larger noise contribution. It is clear, however, that there is a greater difference, relative to the air jet, between LSF and TSF as the separation becomes comparable to the integral lengthscale. The different limiting values of LSF and TSF for the two jets, when $r^* \to \infty$, represent a measure of the difference in anisotropy between these flows. As for the air jet, the slope of the LSF is close to K41 over the IR, whereas the slope of the TSF is discernibly smaller. The TSF derived from (1) approaches the LSF when r^* is comparable to L_u^* (or L_v^*); in (1), when $r^* \to \infty$, the second term on the right-hand side vanishes which makes the TSF then equal to the LSF. The calculated TSF approaches the measured TSF in the IR. This behaviour clearly indicates that the large part of the difference between LSF and TSF is due to the large-scale anisotropy, which is nearly eliminated when using (1). The effect of the small- and large-scale anisotropy on LSF and TSF will be considered in more detail in §§ 6 and 7.

The distributions of $\mathrm{d}(\log\langle(\delta u^*)^p\rangle)/\mathrm{d}(\log r^*)$ are shown in figure 3 for $p = 2$ and

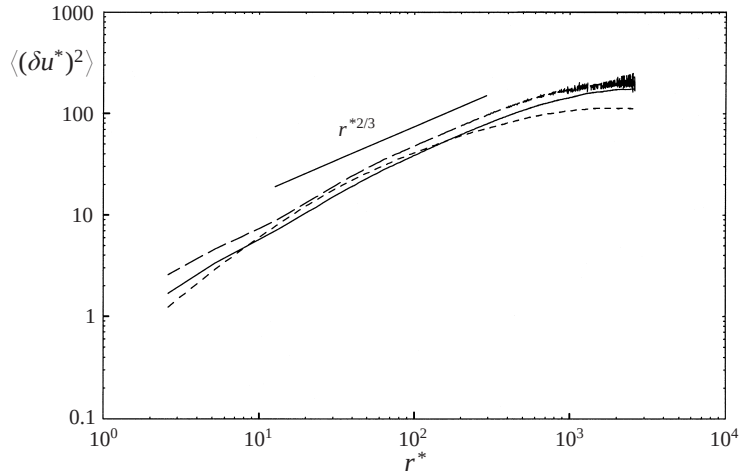

FIGURE 2. Measured second-order LSF and TSF for the water jet. The second-order TSF is also obtained from equation (1). The theoretical slope in the IR is shown. ——, measured LSF; - - -, measured TSF; – –, TSF obtained with (1).

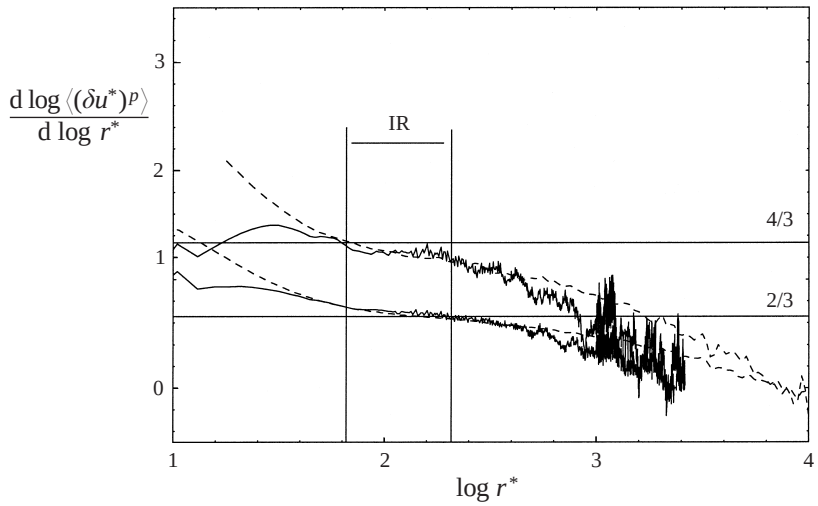

FIGURE 3. Derivative of second-order (below) and fourth-order (above) LSF for the two jets. The amplitude of the IR is bounded by vertical lines. The horizontal lines correspond to the K41 values. ——, water jet; - - -, air jet.

$p = 4$. This presentation allows a more critical appraisal of the IR behaviour of the SFs since plateaux should appear over the IR if the latter is identified with power-laws. Figure 3 shows that there are no plateaux so that the exponents ζ_2^L and ζ_4^L cannot be determined without ambiguity. This result does not contradict either K41 or K62 which were proposed for very large Reynolds numbers; indeed, even when R_λ is of order 10^4, unique values of ζ_2^L (and ζ_2^T) still cannot be identified. Arguably, although the IR may not strictly exist at the present R_λ, figure 3 indicates that there is a range where the variation with respect to r^* of the SF derivatives is small. Also, the ratio $\langle(\delta v)^2\rangle/\langle(\delta u)^2\rangle$ decays only slowly in this range. For these reasons, and because

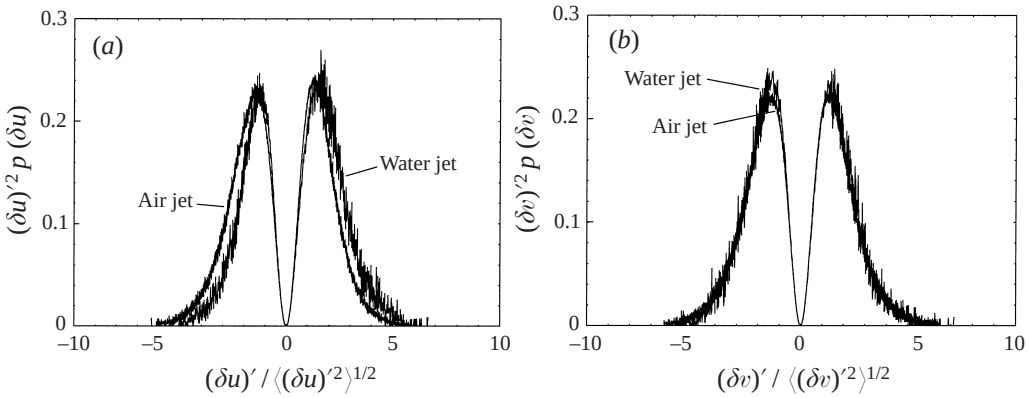

FIGURE 4. Probability density functions of (*a*) longitudinal, and (*b*) transverse normalized velocity increments for the two jets. The p.d.f.s correspond to $r^* = 60$ and are multiplied by $(\delta u)^2$ and $(\delta v)^2$.

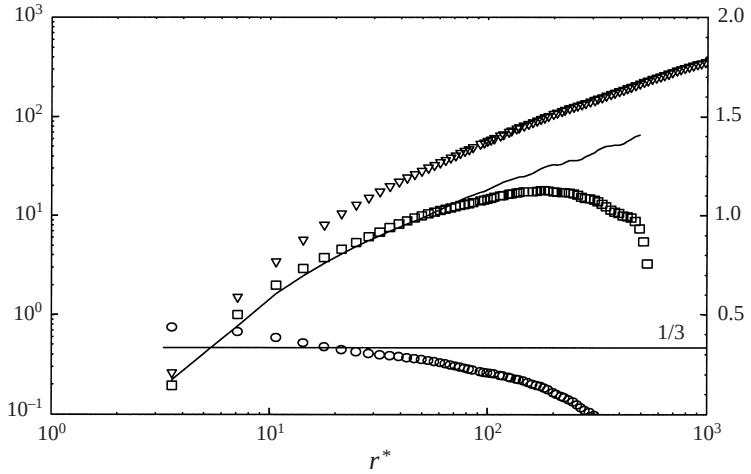

FIGURE 5. Mixed third-order structure functions for the air jet (left-hand scale) and ratio $\langle(\delta u)(\delta v)^2\rangle/\langle(\delta u)^3\rangle$ (right-hand scale). The horizontal line corresponds to the K41 value. ——, $\langle(\delta u)(\delta v)^2\rangle$ with equation (4); □, $\langle(\delta u)(\delta v)^2\rangle$; ▽, $\langle(\delta u)^3\rangle$; ○, $\langle(\delta u)(\delta v)^2\rangle/\langle(\delta u)^3\rangle$.

of the corresponding approximately linear behaviour of $\langle(\delta u)^3\rangle$, we shall continue to refer to the IR.

Figure 3 also indicates that, at approximately the same R_λ, the data from the two jets are in reasonable agreement with each other, especially over the IR. The effect of noise in the LDA data (water jet) seems to be limited to $r^* < 50$. Probability density functions of the longitudinal and transverse velocity increments have been calculated for the two jets at different values of r^*. They are shown in figure 4 for $r^* = 60$, i.e. approximately at the lower limit of the IR. The p.d.f.s have been multiplied by $(\delta u)^2$ or $(\delta v)^2$ to emphasize the behaviour of the tails. The distributions indicate that the number of samples used is adequate for achieving a closure of the integrands associated with $\langle(\delta\alpha)^p\rangle$ (at least up to $p = 6$). The differences between the water and air jets are smaller for the p.d.f.s of δv than the p.d.f.s of δu, because the LDA noise becomes more pronounced as the particles travelling in the streamwise direction have a smaller residence time.

An important and relatively sensitive test of isotropy is given by the following relation (e.g. Monin & Yaglom 1975) between third-order structure functions

$$\langle(\delta u)(\delta v)^2\rangle = \frac{1}{6}\left(1 + r\frac{\partial}{\partial r}\right)\langle(\delta u)^3\rangle. \tag{4}$$

In the IR, the ratio $\langle(\delta u)(\delta v)^2\rangle/\langle(\delta u)^3\rangle$ should be 1/3. For the air jet, (simultaneous measurements of the two velocity components are not available in the water jet), this ratio crosses K41 near the lower limit of the IR (figure 5). In figure 5, the mixed structure function calculated from (4) is in reasonable agreement over the IR with the measured distribution. Both distributions are smaller than $\langle(\delta u)^3\rangle$ for all separations, except perhaps at the smallest r^*, where they converge towards the same behaviour as $\langle(\delta u)^3\rangle$. Although isotropy is approached in the IR, it is strictly not satisfied even at the lower limit of the range. The existence of large-scale anisotropy, which is more pronounced for the water than the air jet, reinforces the previous observation. The difference between LSF and TSF across the whole range of scales, reflects this anisotropy.

5. Different methods for evaluating the IR exponents

The determination of the extent of the IR is important in order to assess whether some of the disagreement, especially for ζ_3^T, between published data may have been caused by the way this range is identified. The following approaches were used.

1. The IR is identified with the region where the third-order LSF increases linearly with r^*, namely $\zeta_3^L \simeq 1$. This is an exact result derived from the Navier–Stokes equations for homogeneous isotropic turbulence at high Reynolds numbers. Scaling exponents of other ($p \neq 3$) structure functions, including the transverse ones, are then determined by fitting data over this range.

2. The IR for the LSFs is identified, as in method 1, with the range over which the third-order LSF increases linearly with r^*. Scaling exponents of the other LSFs are estimated by fitting to the data over this range. However, the IR for the TSFs is identified with the range for which $\zeta_3^T \simeq 1$. This approach lacks rigour.

Variations on the previous methods are provided by applying the extended self-similarity (ESS) method (Benzi *et al.* 1993), i.e. by plotting the pth-order structure function against the absolute third-order structure function and identifying the slope in the range for which the latter is approximately constant. Using the first method and allowing a variation of 2% on the third-order LSF divided by r^*, the IR is estimated to be $60 \leqslant r^* \leqslant 200$ for the two jets. On the other hand, using the second method, the IR for the TSF is shifted to smaller scales and is appreciably smaller ($30 \leqslant r^* \leqslant 70$); over this contracted range, the magnitudes of TSF scaling exponents are expected to be close to those of the LSF exponents.

Another method of estimating the exponents, here identified as method 3, consists of fitting the measured values of $\langle(\delta u)^p\rangle$ or $\langle(\delta v)^p\rangle$ with the relation (e.g. Stolovitzky, Sreenivasan & Juneja 1993; Stolovitzky & Sreenivasan 1995; Grossmann 1995; Meneveau 1996; Antonia, Pearson & Zhou 2000)

$$\langle(\delta\alpha^*)^p\rangle = \frac{a_{\alpha p} r^{*p}}{(1 + b_{\alpha p} r^{*2})^{c_{\alpha p}}}, \tag{5}$$

where $\alpha \equiv u$ or v and $a_{\alpha p}$, $b_{\alpha p}$ and $c_{\alpha p}$ are (possibly flow and Reynolds number dependent) constants and $c_{\alpha p} \equiv \frac{1}{2}(p - \zeta_p^\alpha)$. The fit is applied over a range of r^* which extends from a minimum that could be resolved by measurement (ideally, $r^* \simeq 1$) to

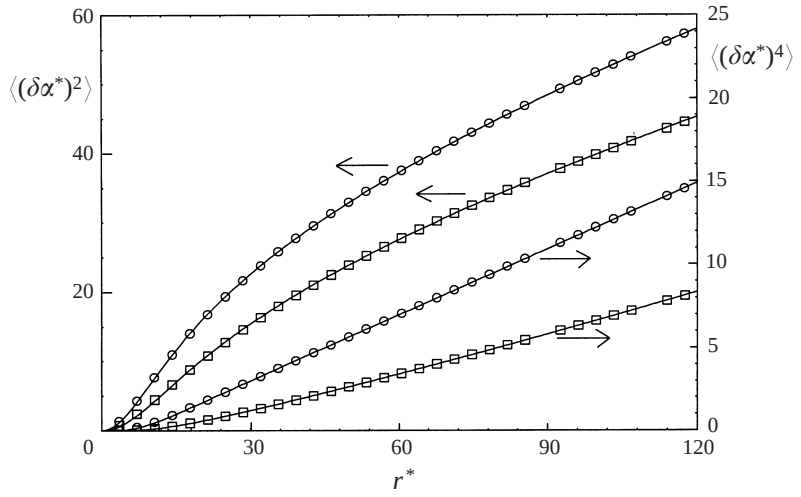

FIGURE 6. Comparison of measured second- and fourth-order LSF and TSF with equation (5) for the air jet. Symbols refer to the measured values; solid lines represent fits to the measurement, using (5). □, LSF; ○, TSF.

a maximum r^*_{max} which corresponds to the outer part of the IR. This method avoids some of the arbitrariness in methods 1 and 2 since, now, only the outer limit of the IR needs to be specified. The quality of the fit (see figure 6) is such that the accuracy of estimating ζ_p is comparable to that using ESS. The main rationale for equation (5), as already pointed out by Stolovitzky *et al.* (1993), is that it asymptotes to the correct behaviour when r approaches zero and when r extends into the scaling range. Kurien & Sreenivasan (2000) considered an analytical extension of (5) which covers the complete range of r from η to L. However, (5) is sufficient for the present purpose of evaluating IR exponents. It was applied only to the air jet data since the DR for the water jet data was noise contaminated. In figure 6, the value of r^*_{max} is taken to be the same as that used in method 1 (a discussion of the effect of the choice of r^*_{max} on a_α, b_α and c_α is given in Antonia *et al.* 2000). The resulting values of ζ_2^L and ζ_2^T are 0.67 and 0.61, whereas ζ_4^L and ζ_4^T are 1.22 and 1.05; the magnitudes of ζ_2^L and ζ_4^T are in good agreement with the local values ($r^* = 120$ or $\log r^* \simeq 2$) indicated in figure 3; an increase in r^*_{max} when applying (5) would result in a decrease in the magnitudes of ζ_α^L and ζ_α^T in a similar manner to figure 3. We note here that the 'constant' exponents provided by ESS should, because of the 'relative' nature of ESS, be interpreted only as 'averages' over the IR.

6. An empirical description of *p*th-order structure functions

In §4, a major portion of the observed differences between LSF and TSF was ascribed to the large-scale anisotropy. The ratio u'/v', which is different in each flow, is an indicator of the energy supplied to the large-scales, since $\langle(\delta u)^2\rangle$ and $\langle(\delta v)^2\rangle$ approach $2u'^2$ and $2v'^2$ when $r^* \to \infty$. A simplistic description of the structure functions is provided by the model proposed below. The model allows estimates of the scaling exponents which take into account the anisotropy of the large scales.

A necessary requirement for a model, as sketched in figure 7, is that it should correctly reproduce the asymptotic behaviour of pth-order structure functions (e.g.

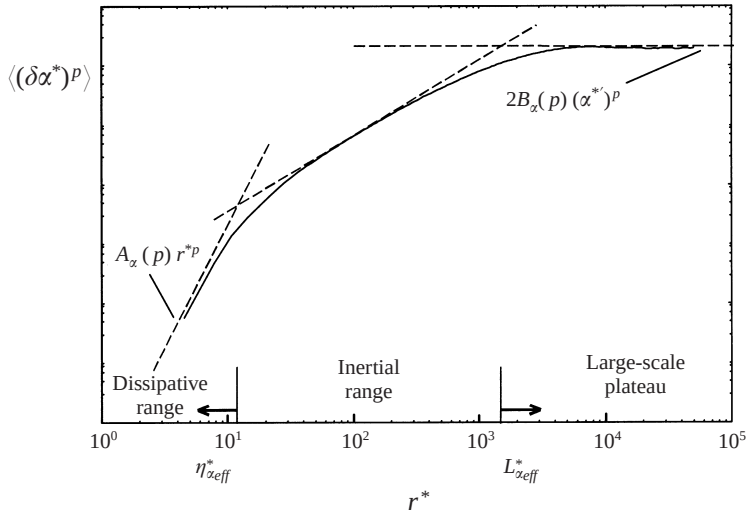

FIGURE 7. Model of the pth-order structure function used to evaluate the scaling range exponents.

Frisch 1995), namely,

$$\left.\begin{aligned}\langle(\delta\alpha^*)^p\rangle &\to A_\alpha(p)r^{*p}, \quad \text{when } r^* \to 0,\\ \langle(\delta\alpha^*)^p\rangle &\to 2B_\alpha(p)\alpha'^{*p} \quad \text{when } r^* \to \infty,\end{aligned}\right\} \tag{6}$$

where $\alpha \equiv u$ or v and the prefactors $A_\alpha(p)$ and $B_\alpha(p)$ depend on the Reynolds number. It is necessary to specify the limiting values for r^*. At the lower end, $r^* \sim 1$, whereas r^* is proportional to L^*_α at the higher end. We adopt Sreenivasan's (1995) suggestion and introduce effective lengthscales (which are multiples of η and L_α), namely, $\eta^*_{\alpha_{eff}}$ $(= \eta_{\alpha_{eff}}/\eta)$ and $L^*_{\alpha_{eff}}$ $(= L_{\alpha_{eff}}/\eta)$. The scaling exponents of the pth-order structure function can then be approximated by

$$\zeta^\alpha_p = \frac{\log\,[2B_\alpha(p)\alpha'^{*p}] - \log\,[A_\alpha(p)\eta^{*p}_{\alpha_{eff}}]}{\log\,(L^*_{\alpha_{eff}}) - \log\,(\eta^*_{\alpha_{eff}})} = \frac{\log C_\alpha(p)}{\log D_\alpha}, \tag{7}$$

where $C_\alpha(p) = (2B_\alpha(p)\alpha'^{*p})/(A_\alpha(p)\eta^{*p}_{\alpha_{eff}})$ and $D_\alpha = L_{\alpha_{eff}}/\eta_{\alpha_{eff}}$. It is of interest to evaluate the relative difference between longitudinal $(\alpha = u)$ and transverse $(\alpha = v)$ exponents

$$\begin{aligned}\frac{\zeta^L_p - \zeta^T_p}{\zeta^L_p} &= \frac{\log C_u(p)/\log D_u - \log C_v(p)/\log D_v}{\log C_u(p)/\log D_u}\\ &= \frac{\log\,[C_u(p)/C_v(p)]}{\log C_u(p)} - \frac{\log\,[D_u/D_v]}{\log D_v} + \frac{\log\,[C_u(p)/C_v(p)]\log\,[D_u/D_v]}{\log C_u(p)\log D_v}.\end{aligned} \tag{8}$$

The evaluations of (7) and (8) require a knowledge of $A_\alpha(p)$ and $B_\alpha(p)$. Assuming isotropy, for $p = 2$ (Frisch 1995)

$$A_u(2) = \tfrac{1}{15}, \quad A_v(2) = 2A_u(2), \quad B_\alpha(2) = 1 \tag{9}$$

and $C_u(2)/C_v(2) = 2(u'/v')^2$. Equation (8) thus explicitly contains information about the ratio u'/v', which is one measure of the large-scale anisotropy. As the degree of anisotropy increases, the magnitudes of the first and third terms on the right-hand side of equation (8) also increase. Further, for isotropic turbulence, $C_\alpha(2) \sim R_\lambda$ and $D_\alpha \sim R_\lambda^{3/2}$. The magnitude of all terms in (8) decreases as R_λ increases. For very large

	$p=2$	$p=4$
ζ_p^L (air)	0.71 (0.67)	1.30 (1.22)
ζ_p^T (air)	0.64 (0.61)	1.10 (1.05)
ζ_p^T (air) (equation (1))	0.68	—[a]
ζ_p^L (water)	0.71	1.26
ζ_p^T (water)	0.58	0.99
ζ_p^T (water) (equation (1))	0.70	—[a]
Error in $\zeta_p^{L,T}$ (air)	$\pm$0.005	$\pm$0.011
Error in $\zeta_p^{L,T}$ (water)	$\pm$0.02	$\pm$0.035

[a]At present, there is no rigorous relation, comparable to (1), between fourth-order LSF and TSF. The empirical relation proposed by Antonia *et al.* (1997*a*) yields values of 1.28 for ζ_4^T (air) and 1.22 for ζ_4^T (water). These are in good agreement with the tabulated values for ζ_4^L (air) and ζ_4^L (water).

TABLE 2. Second and fourth-order LSF and TSF scaling exponents obtained with methods 1 and 3 (within parentheses). Equation (1) has also been used to evaluate TSF exponents for $p=2$.

R_λ, $\log D_u = \log D_v$ and only the first term on the right-hand side of (8) remains. Estimates of $(\zeta_p^L - \zeta_p^T)/\zeta_p^L$ from (8) can be compared with experimental results obtained for different large-scale anisotropies and different Reynolds numbers.

For $p=4$,

$$A_\alpha(4) = \frac{F_{\partial\alpha/\partial x}}{15^2}, \quad B_\alpha(4) = F_\alpha + 3, \tag{10}$$

where $F_\alpha \equiv \langle\alpha^4\rangle/\langle\alpha^2\rangle^2$ is the flatness factor of α. It follows that

$$\frac{C_u(4)}{C_v(4)} = \left(\frac{u'}{v'}\right)^4 \left(\frac{F_u+3}{F_v+3}\right)\left(\frac{F_{\partial v/\partial x}}{F_{\partial u/\partial x}}\right),$$

which depends explicitly on the ratio u'/v'. For $p > 4$, it is possible to derive expressions for $A_\alpha(p)$ and $B_\alpha(p)$, but the constants and factors are more elaborate and difficult to determine.

The values of $\eta_{\alpha_{eff}}$ ($\simeq 10\eta$) and $L_{\alpha_{eff}}$ ($\simeq L_\alpha$), have been chosen, after carefully inspecting the behaviour of several low-order structure functions. These choices (see figure 7) correspond to the upper limit of the dissipative range and the beginning of the large-scale plateau, respectively. However, the results from the model are not very sensitive to slight variations in these quantities.

7. Longitudinal and transverse scaling exponents: Reynolds number dependence

Estimates for second- and fourth-order scaling exponents are summarized in Table 2. There are differences between longitudinal and transverse exponents (about 15% for $p=2$ and 20% for $p=4$). However, when TSF exponents are determined using (1), the difference is strongly reduced (to about 5%). Note that (1) is valid for locally homogeneous and isotropic turbulence and that any intermittency in the LSF is transferred to the TSF. The present results therefore indicate that a large portion of the observed difference between LSF and TSF scaling exponents is caused by a local anisotropy in the IR. The exponents for the air jet determined using method 3, i.e. equation (5), are also very close to those evaluated using method 1 (see table 2). Estimates of uncertainties in ζ_p^L and ζ_p^T are included in table 2. They were obtained

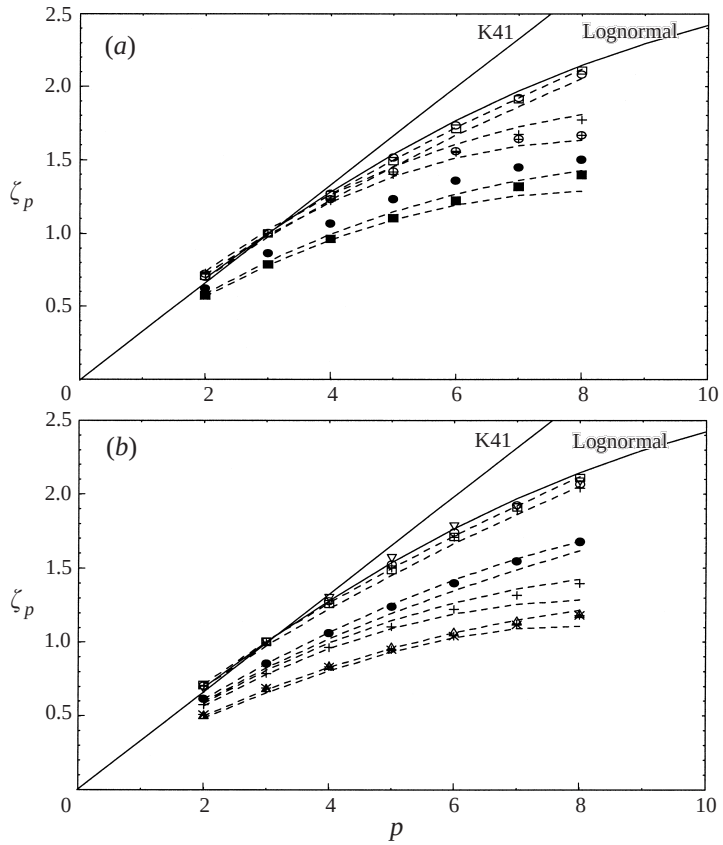

FIGURE 8. (*a*) LSF and TSF scaling exponents for the two jets. - - -, upper and lower error bounds for the water jet (for the air jet, the errors are within the symbol size). □, water jet [filled in symbols, TSF 1; open symbols, LSF 1; +, TSF 2]; ○, air jet [filled in symbols, TSF 1; open symbols, LSF 1; ⊕, TSF 2], where 1 and 2 indicate the method used to determine the scaling range. (*b*) LSF and TSF scaling exponents for the water jet at different Reynolds numbers (only data using method 1 are shown). ▽, LSF for $R_\lambda = 280$; △, TSF for $R_\lambda = 280$; ×, LSF for $R_\lambda = 440$; ∗, TSF for $R_\lambda = 440$; □, LSF for $R_\lambda = 500$; +, TSF for $R_\lambda = 500$; ○, LSF for $R_\lambda = 1000$; ●, TSF for $R_\lambda = 1000$.

after first estimating the errors in $\langle(\delta\alpha)^p\rangle$ ($p = 2, 4$) at the lower and upper limits of the IR. Although there are several sources for these errors and several possible ways of evaluating the errors (e.g. Antonia *et al.* 1982; Anselmet *et al.* 1984), we have used here a slight variant of the method described by Camussi *et al.* (1996). Specifically, the major error ϵ_p in $\langle(\delta\alpha)^p\rangle$ is assumed to be given by the expression $[\{\langle(\delta\alpha)^{2p}\rangle/\langle(\delta\alpha^p\rangle^2\} - 1]^{1/2}/N_{ind}^{1/2}$ where $N_{ind} = \langle U\rangle T_S/2L_{\delta\alpha}$. The integral lengthscale $L_{\delta\alpha}$ associated with $\delta\alpha$ was inferred via the Taylor hypothesis from the integral of the time autocorrelation function of $\delta\alpha$ up to its first zero crossing. The measured magnitudes of the flatness and superflatness factors of $\delta\alpha$ were used for $p = 2$ and 4, respectively.

Table 2 indicates that the exponents are generally smaller (when method 1 is used) for the water jet than for the air jet. The relative difference between longitudinal exponents is about 3% ($p = 4$), compared to about 10% for the transverse exponents ($p = 2$ and $p = 4$). The ratio $(\zeta_p^L - \zeta_p^T)/\zeta_p^L$ is larger for the water than the air jet, confirming the effect the large-scale anisotropy has on the IR. This is further

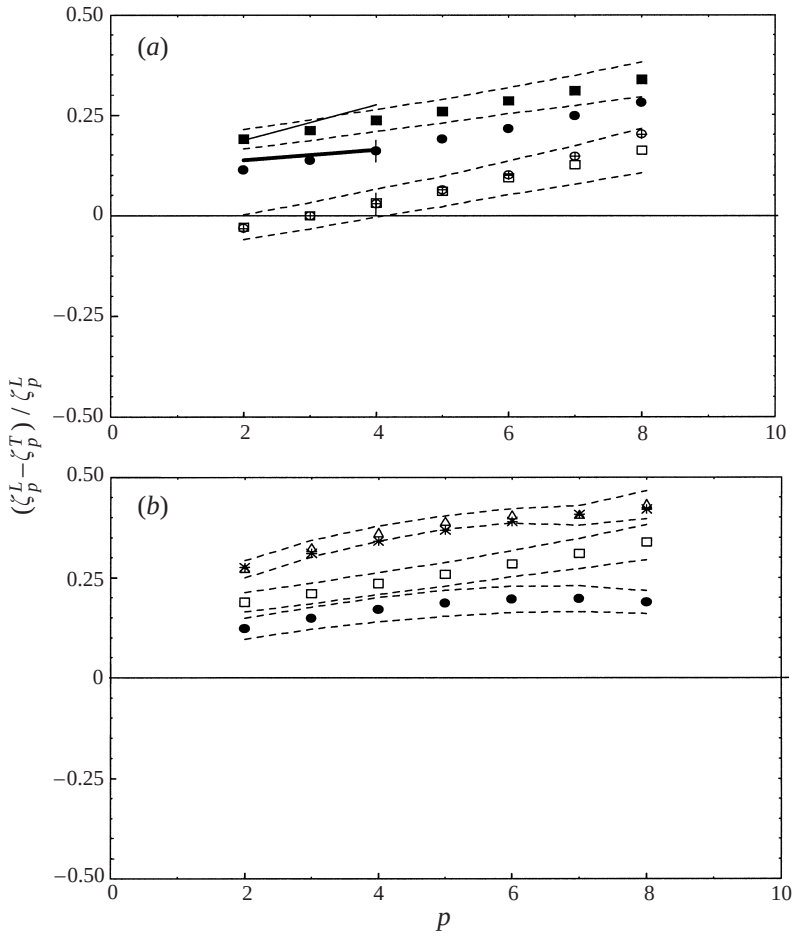

FIGURE 9. (*a*) Relative difference between longitudinal and transverse scaling exponents for the two jets. Estimates from the empirical model for $p = 2$ and $p = 4$ are also shown (thin continuous line for the water jet and thick line for the air jet). - - -, upper and lower error bounds for the water jet (the vertical lines give an indication of the error for the air jet). Water jet [full symbols, 1; □, 2]; air jet [full symbols, 1; ⊕, 2], where 1 and 2 indicate the method used to determine the scaling range. (*b*) Relative difference between longitudinal and transverse scaling exponents for the water jet as a function of the Reynolds numbers (only data using method 1 are shown). △, $R_\lambda = 280$ (1); *, $R_\lambda = 440$ (1); □, $R_\lambda = 500$ (1); ●, $R_\lambda = 1000$ (1).

confirmed by the relative differences calculated from the model of § 6. For the air jet, the ratios are 0.14 and 0.16 for $p = 2$ and 4, respectively (the measured values are 0.10 and 0.15), whereas, for the water jet, they are 0.19 and 0.27 (the measured values are 0.18 and 0.21). This level of agreement underlines the role of u'/v' as a large-scale 'forcing' term.

The difference between the longitudinal and transverse exponents in the two jets can be ascribed to the different global anisotropies in the two flows. This, in turn, reflects differences in initial conditions, although the precise connection between the value of u'/v' at the measurement station and the initial conditions is not understood. Transverse exponents appear to be more affected by the anisotropy than the longitudinal exponents. Exponents were calculated for both flows up to $p = 8$, using methods 1 and 2. To within the uncertainty envelopes indicated in

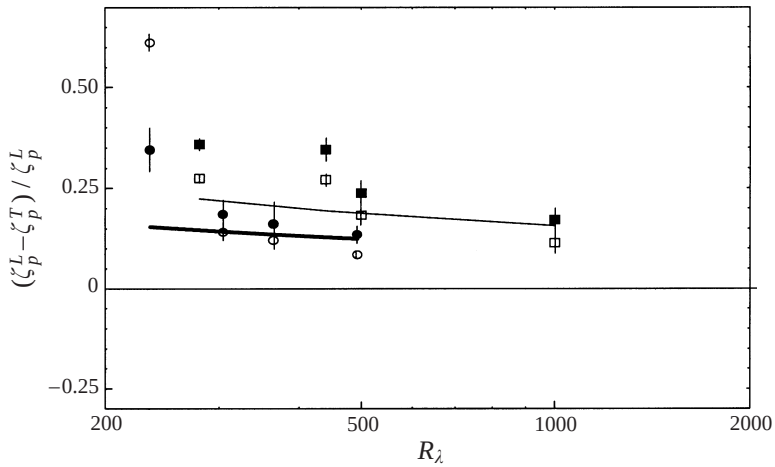

FIGURE 10. Relative differences between longitudinal and transverse second- and fourth-order scaling exponents as a function of the Reynolds number for the two jets. The vertical lines are an estimate of the errors. Open and closed symbols refer to $p = 2$ and $p = 4$, respectively. Estimates from the empirical model for $p = 2$ are also shown (thin continuous line for the water jet and thick line for the air jet). □, water jet; ○, air jet.

figure 8(*a*), there is fairly good agreement between the longitudinal exponents in the two flows. Also, their magnitudes are in reasonable agreement with values reported in the literature, based either on measurement (e.g. Anselmet *et al.* 1984) or DNS data (e.g. Vincent & Meneguzzi 1991; Cao, Chen & Sreenivasan 1996). On the other hand, a difference is observed between the transverse scaling exponents, this difference exhibiting a significant dependence on R_λ (figure 8*b*), where only results for the water jet are shown (at four values of R_λ: 280, 440, 500 and 1000).

The dependence on the order p and on R_λ of $(\zeta_p^L - \zeta_p^T)/\zeta_p^L$ is shown explicitly in figures 9 and 10. A nearly linear variation with respect to p (the slope is about 3%) is observed in figure 9(*a*). Note that these results would virtually collapse if method 2 were used so that the relative difference between longitudinal and transverse exponents would reduce to almost 5% for $p \leqslant 4$ (and less than 10% up to $p = 8$). The results from the model presented in § 6 for $p = 2$ and $p = 4$ are also included. As already noted, the agreement is reasonable in each jet. The trend in figure 9(*b*) supports a reduction in the relative difference as R_λ increases. However, as already noted, even at the highest R_λ, the difference is in the range 10%–20%.

Included in figure 10 are results obtained in the same air jet at $R_\lambda = 235, 305$ and 365 but in a separate investigation. The number of independent samples was smaller than for the present study by a factor of about 15; consequently, the error bars for these three data sets are significantly larger. Notwithstanding the increased uncertainty, the trend in figure 10 is unmistakable. Both the air and water jet data indicate a definite decrease in the ratio $(\zeta_p^L - \zeta_p^T)/\zeta_p^L$ as R_λ increases. In each flow, the decrease is reasonably well represented by the model. The different magnitudes of the ratio in the two flows reflect mainly the different levels of large-scale anisotropy. In each flow, the ratio u'/v' is essentially independent of R_λ (for example, in the water jet, the overall variation is in the range 1.30–1.33) so that the difference in u'/v' between the two flows persists as R_λ increases. It is conceivable that as $R_\lambda \to \infty$, the effect of the anisotropy may be negligible; nonetheless, the results indicate that the effect cannot be ignored for Reynolds numbers at which investigations are carried out.

It is worth discussing the trends indicated by figure 10 in a more general context in view of the variation in published values of $(\zeta_p^L - \zeta_p^T)$, at nominally the same R_λ, obtained in different flows. Zhou & Antonia (2000) compared their measurements of $(\zeta_p^L - \zeta_p^T)$ in low R_λ decaying grid turbulence with DNS results in periodic box turbulence, obtained either at comparable or slightly larger values of R_λ. They noted that, for a fixed value of p, the measured values of $(\zeta_p^L - \zeta_p^T)$ were substantially larger than in the simulations of Boratav & Pelz (1997), who used an unforced flow but with high-symmetry initial conditions, and Grossmann, Lohse & Reeh (1997) who considered forced stationary turbulence. The level of anisotropy, as measured by u'/v', was much smaller in the simulations than in the experiment. Simulations (Kerr, Meneguzzi & Gotoh 2000) for a 1024^3 mesh, with Gaussian white-noise forcing at the lowest band of wavenumbers so as to maintain constant energy, indicated a value of $(\zeta_4^L - \zeta_4^T)$ of about 0.05 at $R_\lambda = 390$. This difference is clearly negligible compared with the present measurements, apparently reflecting the high level of global isotropy in the simulation. Kerr *et al.* also report results from experiments in a return channel and a mixing layer, each obtained at high values of R_λ (3200 and 2100, respectively). The difference $(\zeta_4^L - \zeta_4^T)$ was negligible in both flows although the mixing layer is described as very anisotropic and the channel flow as completely isotropic. It would seem that the effect of increasing R_λ may eventually become more dominant than that associated with any large-scale anisotropy. However, this remark is speculative in view of the documented effect of the mean shear at values of R_λ of the order 10^4 in the atmospheric surface layer (e.g. Sreenivasan & Dhruva 1998; Antonia & Pearson 1999). There is clearly a need for devising experiments and simulations, preferably in the same type of flow but with a means of controlling the global anisotropy.

8. Conclusions

The differences between scaling exponents of longitudinal and transverse velocity structure functions have been investigated experimentally using two round jets, each with slightly different initial conditions. Theoretical arguments, in particular K41, require the longitudinal and transverse exponents to be equal (at least for $p = 2$), whereas the measurements suggest differences between these exponents as high as 15% for $p = 2$, 20% for $p = 4$ and 40% for $p = 8$. These large differences appear to reflect mainly the global anisotropy in the two flows. When the anisotropy is taken into account, for example by enforcing the kinematic constraint of equation (1), the difference between exponents ($p = 2$) is reduced to less than 5%.

The measurements also indicate that the difference between longitudinal and transverse exponents decreases as the Reynolds number increases. The large-scale anisotropy, as represented for example, by the ratio u'/v', seems to be responsible, to a large extent, for the difference between longitudinal and transverse exponents. There is a reduction of about 10% in the relative difference between exponents when u'/v' decreases from 1.32 (water jet) to 1.18 (air jet). The previously reported Reynolds-number dependence of longitudinal, and more especially, transverse exponents is confirmed by the present measurements. Whereas the difference between the longitudinal and transverse exponents is not negligible at the maximum R_λ ($\simeq 1000$) achieved, it is nearly half that at $R_\lambda \simeq 350$.

An empirical model for describing the behaviour of the structure functions has been proposed. The description allows for differences in the magnitudes and lengthscales of longitudinal and transverse velocity fluctuations. It also accounts for the influence of both small and large scales on the behaviour of structure functions in the inertial

range. Results from this model are consistent with the measured relative differences between longitudinal and transverse exponents as well as the R_λ dependence of these exponents.

R. A. A. acknowledges the support of the Australian Research Council. G. P. R. thanks Antonio Cenedese for the continuous help and suggestions and acknowledges the support by the Italian Office for Research (MURST). The help provided by Drs B. R. Pearson, G. Xu and E. Turano is much appreciated.

REFERENCES

Anselmet, F., Gagne, Y., Hopfinger, E. J. & Antonia, R. A. 1984 High-order velocity structure functions in turbulent shear flows. *J. Fluid Mech.* **140**, 63–89.

Antonia, R. A., Ould-Rouis, M., Zhu, Y. & Anselmet, F. 1997*a* Fourth-order moments of longitudinal and transverse velocity structure functions. *Europhys. Lett.* **37**, 85–90.

Antonia, R. A. & Pearson, B. R. 1999 Low-order velocity structure functions in relatively high Reynolds number turbulence. *Europhys. Lett.* **48**, 163–169.

Antonia, R. A., Pearson, B. R. & Zhou, T. 2000 Reynolds number dependence of second-order velocity structure functions. *Phys. Fluids* **12**, 3000–3006.

Antonia, R. A., Satyaprakash, B. R. & Chambers, A. J. 1982 Reynolds number dependence of velocity structure functions in turbulent shear flows. *Phys. Fluids* **25**, 29–37.

Antonia, R. A., Satyaprakash, B. R. & Hussain, A. K. M. F. 1980 Measurements of dissipation rate and some other characteristics of turbulent plane and circular jets. *Phys. Fluids* **23**, 695–699.

Antonia, R. A., Zhou, T. & Romano, G. P. 1997*b* Second and third-order longitudinal velocity structure function in a fully developed turbulent channel flow. *Phys. Fluids* **9**, 3465–3471.

Antonia, R. A., Zhou, T. & Zhu, Y. 1998 Three-component vorticity measurements in a turbulent grid flow. *J. Fluid Mech.* **374**, 29–57.

Benzi, R., Ciliberto, S., Tripiccione, R., Baudet, C., Massaioli, F. & Succi, S. 1993 Extended self similarity in turbulent flows. *Phys. Rev.* E **48**, R29–R32.

Boratav, O. N. & Pelz, R. B. 1997 Structures and structure functions in the inertial range of turbulence. *Phys. Fluids* **9**, 1400–1415.

Camussi, R., Barbagallo, D. & Guj, G. 1997 Experimental analysis of transverse intermittency in a turbulent jet flow. *Exps Fluids* **22**, 268–270.

Camussi, R., Baudet, C., Benzi, R. & Ciliberto, S. 1996 Satistical uncertainty in the analysis of structure functions in turbulence. *Phys. Rev.* E **54**, R3098–R3101.

Cao, N., Chen, S. & Sreenivasan, K. R. 1996 Properties of velocity circulation in three-dimensional turbulence. *Phys. Rev. Lett.* **76**, 616–619.

Chen, S., Sreenivasan, K. R., Nelkin, M. & Cao, N. 1997 A refined similarity hypothesis for transverse structure functions. *Phys. Rev. Lett.* **79**, 2253–2256.

Dhruva, B., Tsuji, Y. & Sreenivasan, K. R. 1997 Transverse structure functions in high Reynolds-number turbulence. *Phys. Rev.* E **56**, 4928–4930.

Frisch, U. 1995 *Turbulence: The Legacy of A. N. Kolmogorov*. Cambridge University Press.

George, W. K. 1989 Self-preservation of turbulent flows and its relation to initial conditions and coherent structures. In *Advances in Turbulence*, Springer.

Grossmann, S. 1995 Asymptotic dissipation rate in turbulence. *Phys. Rev.* E **51**, 6275–6277.

Grossmann, S., Lohse, D. & Reeh, A. 1997 Different intermittency for longitudinal and transversal turbulent fluctuations. *Phys. Fluids* **9**, 3817–3825.

Kerr, R. M., Meneguzzi, M. & Gotoh, T. 2000 An inertial range crossover in structure functions. *Phys. Fluids* (submitted).

Kolmogorov, A. N. 1941 The local structure of turbulence in an incompressible fluid with very large Reynolds number. *Dokl. Akad. Nauk. SSSR* **30**, 301.

Kurien, S. & Sreenivasan, K. R. 2000 Anisotropic scaling contributions to high-order structure functions in high-Reynolds-number turbulence. *Phys. Rev.* E **62**, 2206–2212.

L'vov, V. & Procaccia, I. 1996 The universal scaling exponents of anisotropy in turbulence and their measurement. *Phys. Fluids* **8**, 2565–2567.

Meneveau, C. 1996 Transition between viscous and inertial-range scaling of turbulence structure functions. *Phys. Rev.* E **54**, 3657–3663.

Monin, A. S. & Yaglom, A. M. 1975 *Statistical Fluid Mechanics: Mechanics of Turbulence*. MIT Press.

Noullez, A., Wallace, G., Lempert, W., Miles, R. B. & Frisch, U. 1997 Transverse velocity increments in turbulent flow using the RELIEF technique. *J. Fluid Mech.* **339**, 287–307.

Paret, J. & Tabeling, P. 1998 Intermittency in the two-dimensional inverse cascade of energy: experimental observations. *Phys. Fluids* **10**, 3126–3136.

Pearson, B. R. 1999 Some experiments on small scale turbulence. PhD thesis, University of Newcastle, Australia.

Pearson, B. R. & Antonia, R. A. 1999 R_λ behaviour of 2nd and 4th-order moments of velocity increments and derivatives. In *Turbulence and Shear Flow Phenomena-1* (ed. S. Banerjee & J. K. Eaton), pp. 91–96. Begell House, New York.

Pearson, B. R. & Antonia, R. A. 2001 Reynolds number dependence of turbulent velocity and pressure increments. *J. Fluid Mech.* (submitted).

Romano, G. P., Antonia, R. A. & Zhou, T. 1999 Evaluation of LDA temporal and spatial velocity structure functions in a low Reynolds number turbulent channel flow. *Exps Fluids* **27**, 368–377.

Sreenivasan, K. R. 1995 The energy dissipation in turbulent shear flows. In *Developments in Fluid Dynamics and Aerospace Engineering* (ed. S. M. Deshpande, A. Prabhu, K. R. Sreenivasan & P. R. Viswanath), pp. 159–190. Interline, Bangalore.

Sreenivasan, K. R. & Antonia, R. A. 1997 The phenomenology of small-scale turbulence. *Ann. Rev. Fluid Mech.* **29**, 435–472.

Sreenivasan, K. R. & Dhruva, B. 1998 Is there scaling in high-Reynolds-number turbulence? *Prog. Theoret. Phys. Supp.* **130**, 103–120.

Stolovitzky, G. & Sreenivasan, K. R. 1995 Intermittency, the second-order structure function, and the turbulent energy dissipation rate. *Phys. Rev.* E **52**, 3242–3244.

Stolovitzky, G., Sreenivasan, K. R. & Juneja, A. 1993 Scaling functions and scaling exponents in turbulence. *Phys. Rev.* E **48**, R3217–R3220.

Vincent, A. & Meneguzzi, M. 1991 The spatial structure and statistical properties of homogeneous turbulence. *J. Fluid Mech.* **225**, 1–20.

Water W. van de & Herweijer, J. A. 1999 High-order structure functions of turbulence. *J. Fluid Mech.* **387**, 3–37.

Zhou, T. & Antonia, R. A. 2000 Reynolds number dependence of the small scale structures of grid turbulence. *J. Fluid Mech.* **406**, 81–107.

Zhou, T., Pearson, B. R. & Antonia, R. A. 2000 Comparison between temporal and spatial transverse velocity increments in a turbulent plane jet. *Fluid Dyn. Res.* **28**, 127–138.